LASER INTERFEROMETER GRAVITATIONAL WAVE OBSERVATORY
- LIGO -
CALIFORNIA INSTITUTE OF TECHNOLOGY
MASSACHUSETTS INSTITUTE OF TECHNOLOGY

Technical Note **LIGO-T2600276-v2** 2026/09/25

Cavity-Enhanced Frequency Upconversion of 2 µm Light for Quantum-Efficient Detection

Kato Watsen

California Institute of Technology
LIGO Project, MC100-36
Pasadena, CA 91125
Phone (626) 395-2129
Fax (626) 304-9834
E-mail: info@ligo.caltech.edu

Massachusetts Institute of Technology
LIGO Project, Room NW22-295
Cambridge, MA 02139
Phone (617) 253-4824
Fax (617) 253-7014
E-mail: info@ligo.mit.edu

LIGO Hanford Observatory
Route 10, Mile Marker 2
Richland, WA 99352
Phone (509) 372-8106
Fax (509) 372-8137
E-mail: info@ligo.caltech.edu

LIGO Livingston Observatory
19100 LIGO Lane
Livingston, LA 70754
Phone (225) 686-3100
Fax (225) 686-7189
E-mail: info@ligo.caltech.edu

http://www.ligo.caltech.edu/

Contents

1 Introduction **2**

2 Cavity Alignment and Evaluating Mode Matching **2**

2.1 Optimizing Cavity Alignment 3

2.2 Beam Profiling and Evaluating Mode Matching 4

3 PDH Error Signal and Lock Attempts **4**

3.1 PDH Lock Attempts 4

3.2 EOM Driver Characterization 4

3.3 EOM Phase Modulation and Polarization Dependence 4

3.4 Analytical Error Signal 5

4 Transition to Fiber-Coupled Diode Laser Pump **6**

4.1 Diode Laser Beam Profiling 7

4.2 Optimal Cavity Mode Matching Solution 7

4.3 Cavity Alignment 9

5 Transmittance Characterization of Cavity Mirrors **10**

5.1 Transmittance Characterization with Oscilloscope Measurement 10

5.2 Coherent Detection for Low-Noise Transmittance Measurements 11

5.3 Cavity Mirror Transmittance Results 13

6 Reflection Dip and Error Signal with Revised Input Coupler **13**

6.1 Overcoupled Cavity Measurements 13

7 Conclusion **14**

1 Introduction

The Laser Interferometer Gravitational Wave Observatory (LIGO) detects gravitational waves (GW) by monitoring phase shifts in 1064 nm laser beams with its two interferometers, located at Livingston, Louisiana and Hanford, Washington. The beam is split between the two arms of the interferometer, and movement in arms by GWs induces a differential phase shift between the beams. This creates an interference signal which is detected by a photodetector (PD) at the dark port.

Cryogenic upgrades to LIGO plan to shift the signal field to around 2 µm. In these upgrades, the crystalline silicon testmasses are cryogenically cooled to 123 K, where their thermal expansion coefficent has a zero crossing, mitigating thermoelectric noise in the detector. 2 µm light has low absorption in the silicon test masses compared to high absorption with 1064 nm light. However, photodiodes have low internal quantum efficiency (QE) at 2 µm [1]. Photodetector losses significantly worsen the signal to noise ratio (SNR) of a shot noise limited signal, along with degrading squeezing. However, silicon PDs have high internal QE at 700 nm. By upconverting the 2 µm signal to 700 nm with a 1064 nm pump in a process called sum frequency generation (SFG), the signal can be detected with high QE.

In SFG, the signal and pump fields interact, creating the upconverted field at the signal and pump sum frequency. $\chi^{(2)}$ nonlinear media, such as $LiNbO_3$ and KTP, facilitate this process. The SFG conversion efficiency depends on phase matching and the pump intensity. Cavity-enhanced SFG increases the intracavity pump field, leading to higher conversion efficiency. For doubly resonant cavities, 75% external QE for 1550 nm to 532 nm upconversion [2] has been reported. In this experiment, the pump field will be resonant in the bow-tie cavity with the signal field single-pass to upconvert the signal while minimizing cavity-coupled noise.

This report troubleshoots the Pound-Drever-Hall (PDH) lock for the pump-resonant cavity, an issue inhibiting SFG. The mode matching of an adopted experimental setup using a Nd:YAG non-planar ring oscillator (NPRO) pump is verified, and the electro-optical modulator (EOM) driver is characterized. The experimental setup then transitioned to a fiber-coupled diode laser pump to mitigate astigmatism, mode quality issues, relaxation oscillations, and cavity alignment limitations. The cavity mirrors' transmittances were characterized to reconcile the discrepancy between the analytical and measured PDH error signal, and a new input coupler was found to overcouple the cavity. This increased the PDH error signal SNR to 45 dB, enabling cavity locking.

2 Cavity Alignment and Evaluating Mode Matching

Achieving pump resonance in the cavity requires spatial alignment and mode matching the cavity's eigenmode. Fig. 1 shows the experimental setup for aligning, mode matching, and PDH locking the pump to the cavity prior to inserting the PPLN crystal and introducing the 2 µm signal. The FSR of the cavity is $\Delta\nu = 393\,\mathrm{MHz}$, linewidth $\delta\nu = 500\,\mathrm{kHz}$, and finesse $\mathcal{F} = 786$.

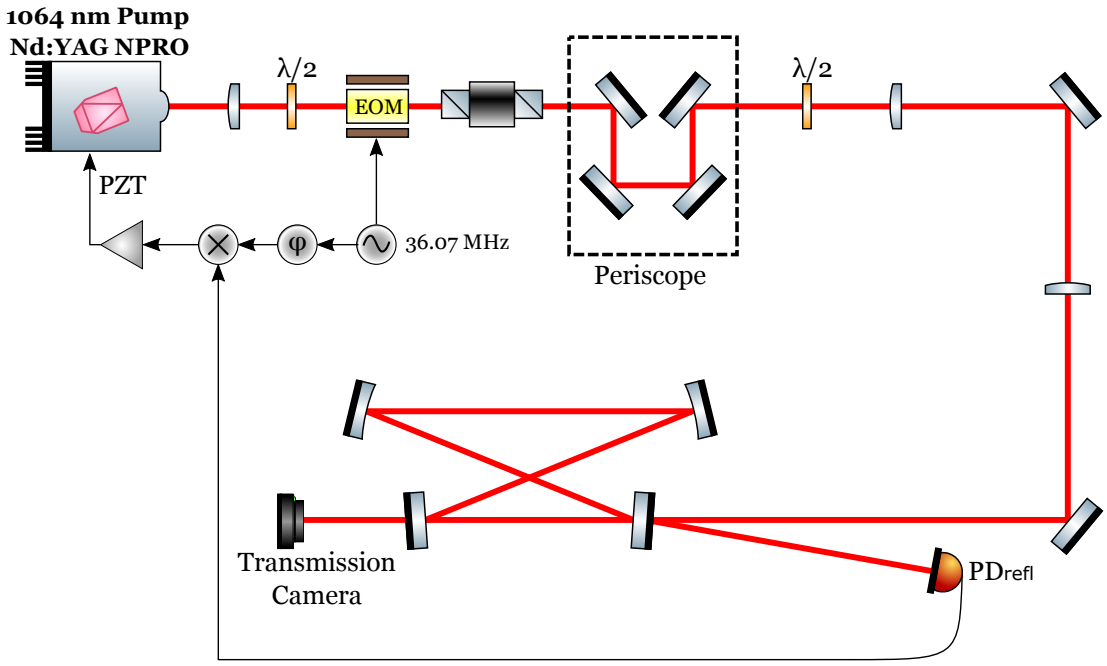


Figure 1: Experimental setup for pump cavity-enhancement . The 1064 nm pump is aligned and mode matched to the bow-tie cavity. PD_{refl} (New Focus 1811) measures the reflected pump off the input coupler for PDH locking the pump to the cavity. The transmission camera records the transmitted pump through the output coupler for cavity alignment. The input and output couplers have 1000 ppm transmission for 1064 nm. The two trichroic curved mirrors have $R = 0.2\,\mathrm{m}$ and 3000 ppm transmittance for 1064 nm. The trichroic mirrors are AR (anti-reflective) for 2000 nm and 700 nm. The periscope situates the beam in the vacuum chamber with the mode matching and cavity optics.

2.1 Optimizing Cavity Alignment

The pump beam was well aligned and fairly mode matched to the cavity at the start of the project. The transmission camera showed flashing of TEM_{00} and higher order modes. This indicates that the Gaussian and higher order modes are partially resonant in the cavity. Due to spatial constraints, there was only one mirror before the input coupler for cavity alignment, thus the mirror prior to the input coupler (IC) and the first curved mirror were empirically optimized to maximize the TEM_{00} viewed on the transmission camera. There was no noticeable improvement in cavity flashing. This can be attributed to the fact that adjusting the curved mirror also changes the required alignment of the input coupler, causing the optimization to not converge effectively.

2.2 Beam Profiling and Evaluating Mode Matching

Pickoff mirrors redirected the beam to a DataRay Beam'R2 scanning slit beam profiler for characterizing the beam profile before the input coupler. The beam profiler measured the intensity distribution of the pump beam along the trajectory. Fitting the Gaussian beam parameters to the measured intensity distribution, $q_h = -1.64 + i4.77$ in relative to the input coupler for the horizontal axis. The cavity eigenmode is $q_{cav} = -1.9783 + i5.1174$ in relative to the input coupler. The mode mismatch for the horizontal axis is 0.25 %. The vertical q-parameter was $q_v = 1.11 + i7.10$ in with a mode mismatch of 8.4 % for the vertical axis. Therefore, the current mode matching is sufficient for coupling the pump into the cavity despite the astigmatism.

3 PDH Error Signal and Lock Attempts

3.1 PDH Lock Attempts

60 dB of digital gain amplified the error signal to the same 100 mV amplitude where previous lock attempts were achieved. At this comparable signal level, the previous loop filter was applied; however, the system never acquired lock while actuating the PZT due to the low error signal SNR of around 2.

3.2 EOM Driver Characterization

The low error signal drove us to characterize the EOM and driver. The EOM presents a 10 pF input impedance to the driver. The driver creates a resonant LC amplifier with a variable inductor to tune the resonance frequency. This was characterized as 36.07 MHz with 4.33 dB of gain at the EOM monitor output which is buffered from the EOM output. The EOM monitor output is -37.45 dB from the EOM output. Therefore, the EOM driver provides 41.78 dB of gain whereas the specified gain is 43.8 dB [3] — a discrepancy of about 2 dB. A 190 mVpp EOM driver modulation for a New Focus 4004 EOM corresponds to a modulation index of 175 mrad compared to 225 mrad with the specified gain. Fig. 2 plots the frequency response of the EOM driver adjusting for the known conversion gain between the EOM monitor and output ports. This confirms that the EOM was driven at the correct resonance frequency.

3.3 EOM Phase Modulation and Polarization Dependence

An asymmetric Michelson interferometer (MI) is a phase modulation (PM) discriminator with fringe spacings at $\Delta\nu = \frac{c}{2\Delta L}$ where ΔL is the path length increase in the longer arm. We aligned a MI prior to the periscope to the vacuum chamber with a path length increase of 16 in, creating a phase excursion of $2\pi f \Delta L/c$. To lock the MI mid-fringe, the phase excursion must be at least $\pi/2$ which corresponds to a frequency shift of 188 MHz. The PZT actuator has a FM gain of 1 MHz/V and its driver outputs 100 V at maximum; therefore, the MI cannot be locked with the PZT control to characterize the EOM PM frequency response.

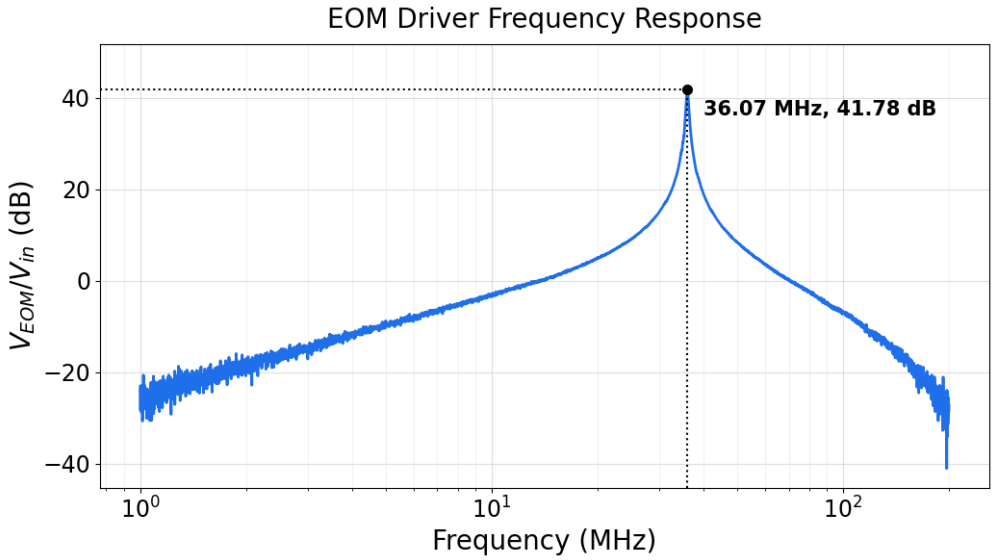


Figure 2: EOM driver characterization. The frequency response sweep was taken at the buffered EOM monitor port and calibrated with the known conversion gain between the monitor and EOM output port.

However, the spectrum analyzer can measure the relative amplitude of the sidebands for various polarizations through the EOM.

When modulating the EOM driver with a 36.07 MHz signal at 190 mVpp, there was a −45 dBm signal at 36.07 MHz on the spectrum analyzer when transmitting s-polarized light through the EOM with a polarizer replacing the half-wave plate. For p-polarized light, the signal dropped to -69 dBm. For 45 degrees of rotation from s-polarization, the signal was -44 dBm. Here, blocking one arm of the MI reduced the signal which is indicative of RAM when the polarization is not properly rotated. We retained the polarizer in place of the half-wave plate to ensure s-polarization through the EOM.

3.4 Analytical Error Signal

Assuming the cavity is lossless and perfect mode matching, the frequency response for the reflected pump field from the bow-tie cavity is given by

$$F(\omega) = \frac{E_{refl}}{E_{in}} = \frac{r_1(r_2^2 e^{-i\omega/\Delta\nu} - 1)}{1 - r_1^2 r_2^2 e^{-i\omega/\Delta\nu}}, \tag{1}$$

where r_1 and r_2 are the reflection coefficients of the flat and curved mirrors, respectively, and $\Delta\nu$ is the FSR of the cavity. By modulating the phase of the pump field at Ω, [4] provides the reflected pump field power as

$$\begin{aligned} P_{\text{refl}}(t) = 2P_0 J_0(\beta) J_1(\beta) [&\text{Re}\{F(\omega)F^*(\omega+\Omega) - F^*(\omega)F(\omega-\Omega)\}\cos(\Omega t) \\ &+ \text{Im}\{F(\omega)F^*(\omega+\Omega) + F^*(\omega)F(\omega-\Omega)\}\sin(\Omega t)] + \text{DC} + \ 2\Omega \text{ terms} \end{aligned} \tag{2}$$

where β is the modulation index, Ω is the phase modulation frequency, and P_0 is the incident optical power, and J_n is the nth order Bessel function of the first kind.

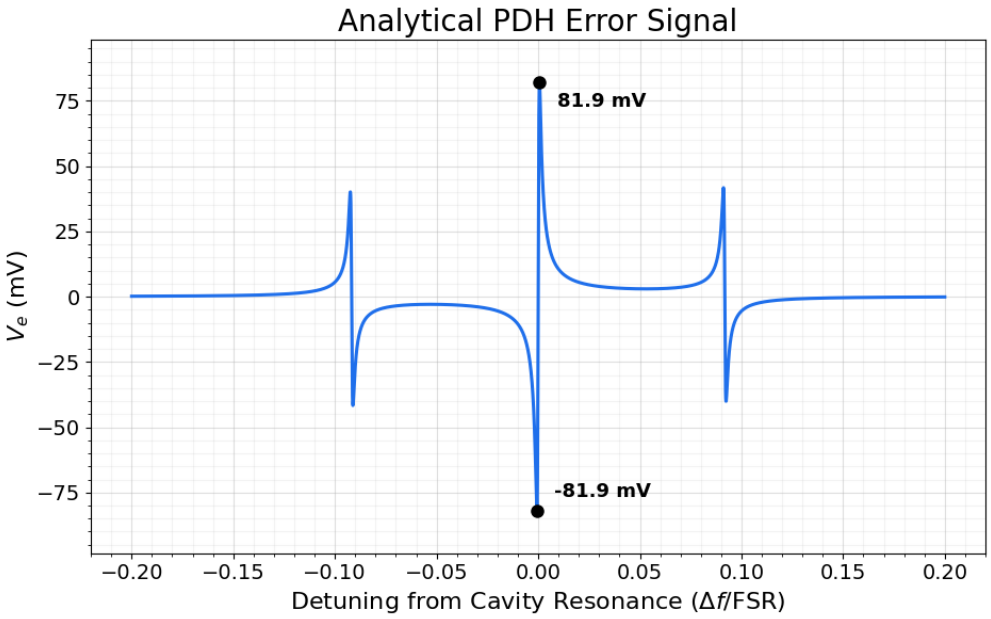


Figure 3: Analytical PDH error signal for the bow-tie cavity with flat and curved mirror transmittances of 1000 ppm and 3000 ppm, respectively.

A photodetector with responsivity R and transimpedance gain Z_T, detects this field and demodulates it at Ω with a mixer and low-pass filter to produce the PDH error signal. For $\Omega >> \delta\nu$, the imaginary part error signal term is much larger than the real part, thus demodulating with $\cos(\Omega t)$ recovers the error signal. The Moku:Pro mixer divides the amplitude of the demodulated signal by 2. The error signal viewed after low-pass filtering for the DC mixer component on a Moku:Pro with 50 Ω input impedance is

$$V_{\mathrm{e}}(\omega) = \sqrt{2} P_0 J_0(\beta) J_1(\beta) R Z_T \,\mathrm{Im}\{F(\omega)F^*(\omega+\Omega) + F^*(\omega)F(\omega-\Omega)\}. \tag{3}$$

For the New Focus 1811 photodetector with 70 μW of reflected pump power after ND filtering, phase modulation at 36.07 MHz with the specified $\beta = 0.225$ results in a PDH error amplitude of 81.9 mV. Fig. 3 plots the error signal for the bow-tie cavity with the given parameters relative to the cavity resonance.

The analytical error signal amplitude is nearly three orders of magnitude larger than the measured error signal of 100 μV. This could be a result of misalignment of the pump to the cavity, mode mismatch, or mirrors deviating from their specified transmittance.

4 Transition to Fiber-Coupled Diode Laser Pump

Due to the astigmatism, mode quality, and deprecation of the Nd:YAG NPRO laser impeding cavity coupling, the experiment is switching to a RIO 1064 nm fiber-coupled diode laser in a new lab space. Since the experiment will have to be rebuilt, this provides an opportunity for revising the existing setup. In this revision, two mirrors precede the input coupler to decouple the positional and angular degrees of freedom for pump alignment into the cavity.

Since the experimental layout is unconstrained, new mode matching design can be designed for robustness against lens placement variations. Fig. 4 shows the revised experimental setup using a RIO fiber-coupled diode laser as the 1064 nm pump.

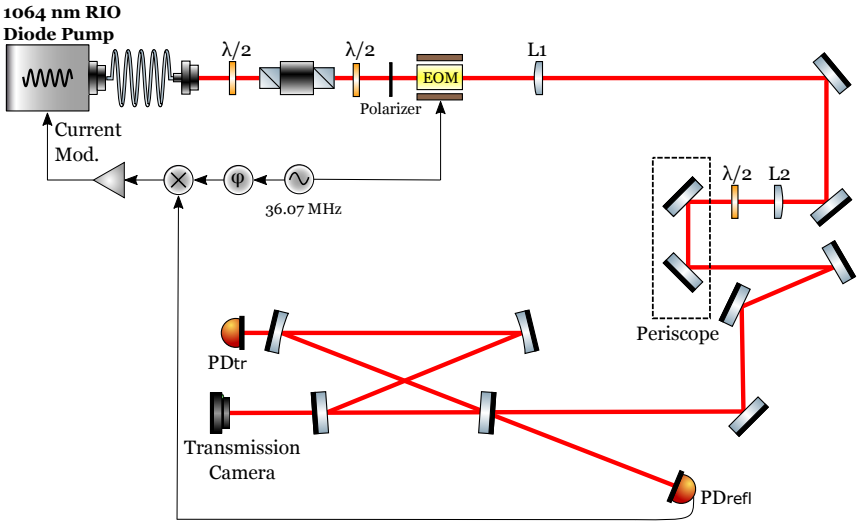


Figure 4: Experimental Setup for PDH Locking a 1064 nm RIO Fiber-Coupled Diode Laser Pump. The polarizer selects s-polarization through the EOM to mitigate residual amplitude modulation (RAM). The periscope elevates the beam to the vacuum chamber with the cavity optics for cavity-enhanced SFG.

4.1 Diode Laser Beam Profiling

The beam was profiled with the scanning slit beam profiler after the EOM to fit the Gaussian beam parameters for the horizontal and vertical beam axis. Fig. 5 shows the fitted Gaussian beam parameters for the sampled beam radius. The horizontal q-parameter relative to the EOM is $q_h = -6.84 + i23.67\,\text{cm}$ and the vertical q-parameter is $q_v = -7.37 + i19.64\,\text{cm}$. The RMS error of the measured beam radii to the Gaussian beam fit was 38.5 µm for the horizontal axis and 29.0 µm for the vertical axis.

4.2 Optimal Cavity Mode Matching Solution

The cavity retained the same geometry and mirrors as the previous setup — with a cavity eigenmode q-parameter of $q_{cav} = -5.00 + i10.94\,\text{cm}$ relative to the input coupler; the input coupler was 233 cm after the EOM. With this beam characterization, I designed a two lens mode matching solution for the cavity mode.

The mode matching efficiency is defined as

$$\eta = \frac{4\,\text{Im}\{q_0\}\,\text{Im}\{q_{cav}\}}{|q_0 - q_{cav}^*|^2}, \tag{4}$$

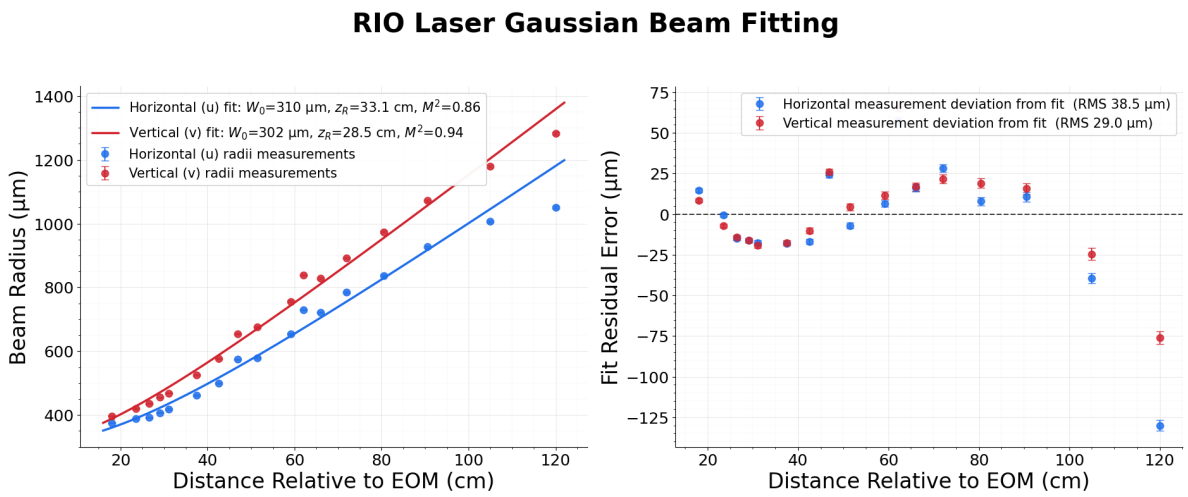


Figure 5: Gaussian beam parameter fitting to measured beam radii. 20 samples at each location were averaged for the radii measurements. Measurement uncertainty was taken as the quadrature sum of the beam profiler's radii accuracy (0.05 % of scan range) and the standard error of beam radius samples at each location; the average measurement uncertainty was ±2.08 µm. The fit residual error plot shows the difference between radii measurements to the Gaussian beam fit.

where q_0 is the q-parameter of the pump beam at the input coupler and q_{cav} is the cavity eigenmode q-parameter.

For a system ABCD matrix to the cavity, M, that propagates the beam from the profiled EOM with q_{EOM} to the cavity input coupler, the q-parameter at the input coupler is given by

$$q_0 = \frac{Aq_{EOM} + B}{Cq_{EOM} + D}. \tag{5}$$

The optimization problem for mode matching is formulated as:

$$\begin{aligned} \text{maximize: } & \eta(f_1, f_2, d_1, d_2, q_{EOM}, q_{cav}) \\ \text{subject to: } & f_1, f_2 \in \text{available lenses} \\ & d_1 < d_2 \\ & d_1 > \text{exclusion boundary 1} \\ & d_1 + d_2 < \text{exclusion boundary 2.} \end{aligned} \tag{6}$$

f_1 and f_2 are the focal lengths of the two lenses, and d_1 and d_2 are their respective positions relative to the EOM. The lower bound of the lens positions is constrained by the first exclusion zone, and the upper bound is constrained by the second exclusion zone. In the experiment, these exclusion zones are set by the EOM mount and the periscope mirror.

A vectorized grid search of the lens focal lengths and positions found the collection of two lens candidate solutions that yielded $\eta = 1$. These candidates were ranked by their mode matching sensitivity to deviations in lens positions and length to the cavity. The optimal solution was taken as the solution with $\eta = 1$ with the maximum mean deviation

in lens positioning and cavity length that causes a 5% decrease in η. The search space was constrained by the available lenses and spatial constraints on the optical table. The optimum mode matching solution was a $f = 1000\,\text{mm}$ lens placed 12.0 cm after the EOM and a $f = 572.7\,\text{mm}$ lens placed 149.6 cm after the EOM.

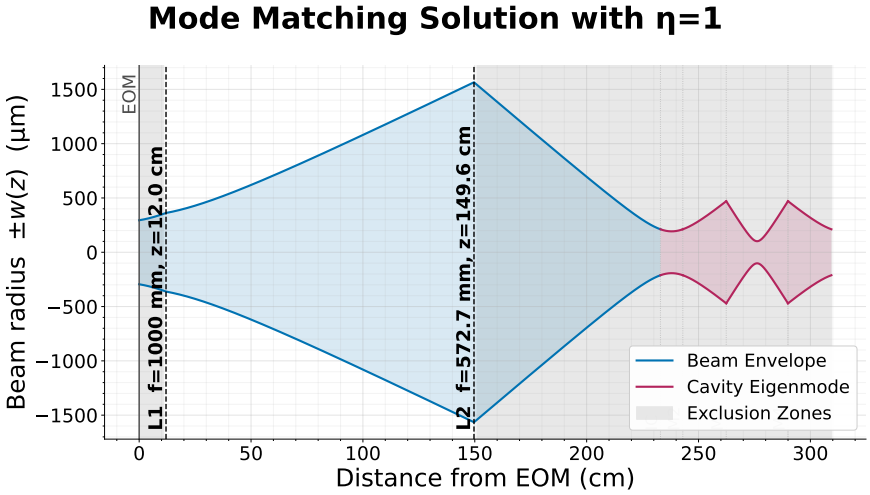


Figure 6: Mode matching lenses focal lengths and positions for robustness against lens positioning and cavity length deviations.

Fig. 6 shows the optimal mode matching solution and Fig. 7 shows the robustness of the solution to lens positioning and cavity length deviations. This solution can withstand a 17.0 cm displacement in the first lens, 6.13 cm displacement in the second lens, or a 5.0 cm displacement in the length to the cavity before a 5% decrease in mode matching efficiency.

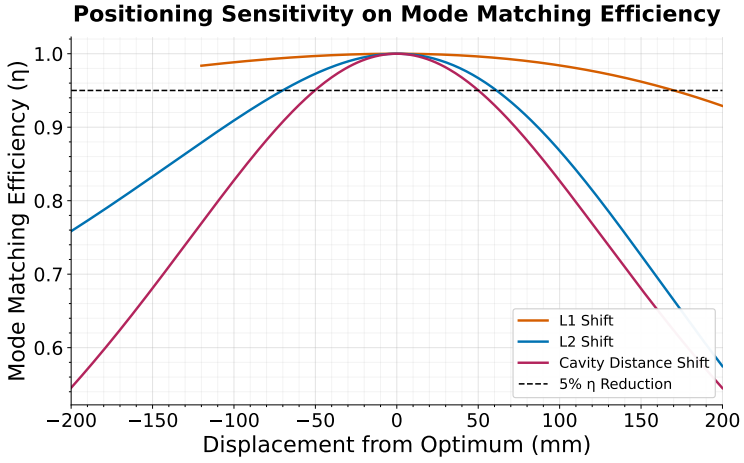


Figure 7: Mode matching solution sensitivity to displacement in lens position and cavity length.

4.3 Cavity Alignment

With the input coupler removed, the pump beam was centered on the second flat mirror with the two mirrors prior to the input coupler. Then, each of the cavity mirror angles

were adjusted to center the reflection on the following cavity optic until the reflection off the second curved mirror was intersecting the incident beam at the input coupler's center. The angles of the two flat cavity mirrors and incident beam mirrors were adjusted to maximize the flashing of the TEM_{00} mode on the transmission camera.

No reflection dips were observed on the reflection photodetector, although the transmission camera showed strong flashing of the TEM_{00} mode with higher order modes. We were unable to observe a PDH error signal on the reflection photodetector when modulating the pump with the EOM. Since alignment to the cavity axis should improve with decoupled degrees of freedom with the cavity alignment mirrors, it is suggestive that the cavity mirrors have an anomalous transmittance.

5 Transmittance Characterization of Cavity Mirrors

To reconcile the discrepancy between the analytical and measured PDH error signal, we characterized the transmittance of the cavity mirrors. Low frequency noise of the laser intensity and thermal drifts hinder using the DC readout of optical power meters for low transmittance mirrors. Modulating the incident beam with an optical chopper upconverts the transmitted power to a higher frequency where the noise is slowly varying compared to the fundemental frequency of the detected signal.

5.1 Transmittance Characterization with Oscilloscope Measurement

An optical chopper applies a square wave intensity modulation, extinguishing the power by periodically blocking the beam. The optical chopper used provided an intensity modulation with a fundemental frequency between 50-100 Hz. The device under test (DUT) was placed in the path between the chopper and an amplified silicon photodetector (Thorlabs PDA36A). The incident optical power was increased and a gain of 40 dB was applied to the PD output to overcome the digitalization noise of the Moku when measuring the DUT. A reference trace was taken with 5.08 mW directly incident on the photodetector with no PD gain. The PD voltage was measured using the Moku's oscilloscope instrument.

The measured peak-to-peak voltages were 1.03 V, 19.6 mV, and 5.17 mV for the reference, flat mirror, and curved mirror, respectively. The flat mirror had 72 mW incident and the curved mirror had 78 mW incident. To find the transmittance, the detected voltage (V_{tr}) was normalized to the reference voltage (V_{ref}), scaling by the PD gain (K_{PD}) and incident optical power with Eq. (7). P_{inc}^{tr} is the incident optical power on the DUT and P_{inc}^{ref} is the incident optical power with no DUT.

$$T = \frac{V_{tr}/(K_{PD} \cdot P_{inc}^{tr})}{V_{ref}/P_{inc}^{ref}} \tag{7}$$

With this method, the transmittance of the flat mirror was 13.4 ppm and the curved mirror was 3.27 ppm. These transmittances were much lower than the expected values. This drove us to find the datasheets for the mirrors. The reflectance of the flat mirror was listed as

greater than 99.99%, suggesting a transmittance less than 100 ppm. This is an order of magnitude lower than the previously expected transmittance. The Thorlabs E03 coating on the curved mirror was specified with a lab-measured reflectivity of 99.7% which has a transmittance of 3000 ppm. The measured curved mirror transmittance was three orders of magnitude lower than the specified value. This discrepancy launched me to take a more accurate measurement of the cavity mirror transmittance should be taken before its value can be considered relaible.

5.2 Coherent Detection for Low-Noise Transmittance Measurements

A SR830 Lock-in Amplifier with a lower input noise of $6\,\mathrm{nV}/\sqrt{\mathrm{Hz}}$ can improve the confidence of the measurement. Since instrument has a lower input referred noise compared to the oscilloscope, the PD amplification is not required to resolve the signal. The lock-in amplifier demodulates both the in-phase and quadrature components of the signal, and it provides the computed amplitude and phase on its readout. The SR830 had a 1 Hz low-pass filter with a 24 dB/oct roll off after demodulation, along with notch filters at 60 and 120 Hz. The optical chopper provided a 270 Hz intensity modulation as a local oscillator (LO).

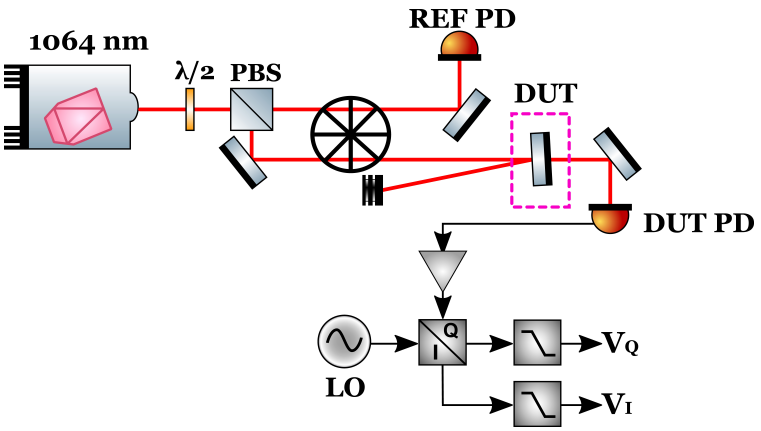


Figure 8: Experimental setup for coherent detection of the cavity mirror transmittances with a SR830 Lock In Amplifier. The SR540 optical chopper modulates the incident beam at 270 Hz. The transmitted signal from the DUT PD is demodulated with a lock-in amplifier at the chopper frequency. The REF PD measures the incident power on the DUT to normalize against intensity drift over the course of measurement. The lock in amplifier displays the quadrature sum of the in-phase and quadrature components as the amplitude, decoupling the LO phase from the measurement.

To mitigate the effect of laser intensity drift over the course of measurement, a reference PD measured the incident power on the DUT. A PBS divided the beam into two paths: the majority of the light, reflecting off the PBS, went to the DUT while the minority was incident on the reference PD. The reflected light was s-polarized: to test the transmittance for p-polarization, I inserted a half waveplate and PBS prior to the DUT to filter for p-polarization. The setup of this setup is shown in Fig. 9.

The lock-in amplifier demodulated the transmitted signal from both the DUT and the REF PD at the LO provided by the SR540. The lock-in amplifier has a PLL that extracted the

fundamental from the LO, measuring the power contained in the first harmonic of the PD signal. The gain of the lock-in amplifier was adjusted to maximize its sensitivity without saturation. The transmittance was calculated by normalizing the transmitted signal by the reference signal, along with normalizing against systematic power imbalance with a control in (8). In this formula the superscript denotes whether the measurement was taken with a DUT or control in the path, and the subscript denotes the PD measuring the signal.

$$T = \frac{V_{dut}^{dut}/V_{ref}^{dut}}{V_{dut}^{control}/V_{ref}^{control}}, \tag{8}$$

The PD has a 94.9 nV/$\sqrt{\text{Hz}}$ noise refered to the input of the SR830. This is independent of the lock-in amplifier's 6 nV/$\sqrt{\text{Hz}}$. The quadrature sum of 95.1 nV/$\sqrt{\text{Hz}}$ is the total noise at the input of the lock-in amplifier. Assuming the lock-in amplifier PLL has no phase jitter, this noise is integrated over the effictive noise bandwidth (ENBW); at a 1 Hz low pass filter with a 24 dB/oct roll off, the ENBW is 78 mHz. The integrated input refered noise is $V_n = 26.6\,\text{nV}$.

The demodulated RMS voltage in the frequency of the square wave is $V_t = 0.45 \cdot R \cdot Z \cdot P_{inc} \cdot T$. R and Z are the responsitivity and transimpedance of the PD at 0.3 A/W and 1.51 kOhm, respectively. 0.45 is the voltage distributed in the fundemental frequency of the square wave. P_{inc} is the incident optical power on the DUT. For 30 mW incident on the DUT, the voltage from the PD to the SR830 is $V_t = (6.12\,\text{V}) \cdot T$. Thus, the SNR of the signal is Vt/Vn. This suggests that this method can measure a transmittance of 1 ppm with an SNR of 230.

The transmittance was measured from 0 to 10° angle of incidence (AOI) for s and p-polarization. The mirrors measured were the flat (LAYERTEC 143580) cavity mirror, curved (Thorlabs CM254P) cavity mirror, and a candidate input coupler (Y1-1025-0) as an option to overcouple the cavity.

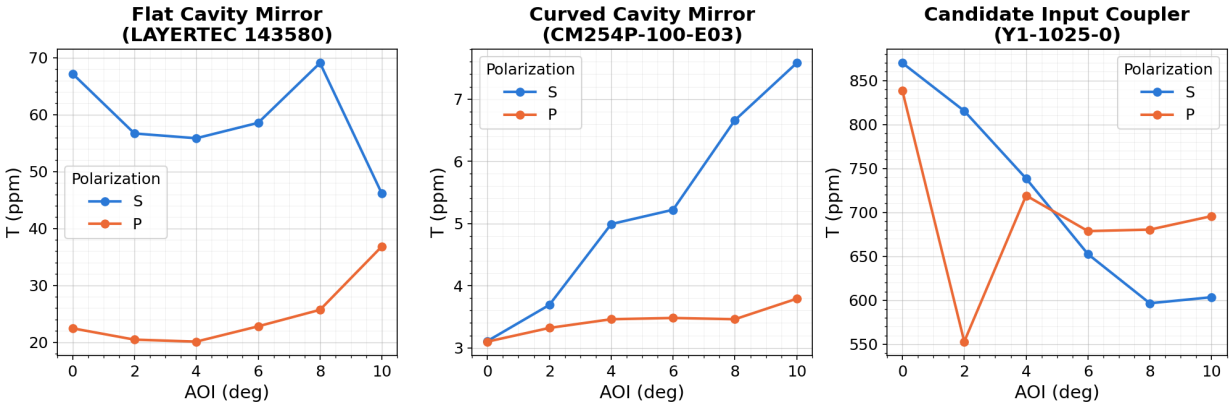


Figure 9: Transmittance characterization result of the cavity mirrors and a Y1-1025-0 flat input coupler replacement candidate. At an 8° angle of incidence, the transmittances were 69.1 ppm and 6.7 ppm for the flat and curved cavity mirrors for s-polarization, respectively. The Y1-1025-0 flat mirror replacement candidate had a transmittance of 596.6 ppm at an 8° for s-polarization.

5.3 Cavity Mirror Transmittance Results

Fig. 9 shows the result of the transmitance measurements with the coherent detection method. The AOI on the cavity mirrors are all close to 8°, so the measurements at these AOI will be emphasized. The flat cavity mirror had different transmittances between the two polarizations; however, both are close to the expected 100 ppm at 8° AOI. For s-polarization, the transmittance was 69.1 ppm at 8°. The discrepancy between the polarization transmittance at normal incidence could be due to a birefringent coating on the mirror, causing a different reflection coefficient for each polarization. The curved cavity mirror had a transmittance of 6.7 ppm and 3.5 ppm for s and p-polarization, respectively, at 8°. This result corroborates the prior measurement, concluding that the curved mirror transmitances is three orders of magnitude lower than the expected 3000 ppm.

A 6.7 ppm curved cavity mirror brings the cavity closer to critically coupled than undercoupled, leading to a larger PDH error than the analytical expectation in Fig. 3. This brings the PDH error signal measurement in further disagreement with the analytical expectations. However, the cavity finesse is around 41,000 with the measured transmittance. This brings the cavity linewidth to 9.6 kHz. The Nd:YAG NPRO laser has lower phase noise than the RIO diode laser by nature, so we were able to resolve a PDH error signal as it crosses through the caivty resonance. With the diode laser, however, we were unable to resolve a PDH error signal. This is consistent with having a narrower cavity linewidth where noise and transient cavity dynamics impede resolving the error signal.

The candidate Y1-1025-0 mirror has a transmittance of 596.6 ppm at 8° for s-polarization, making it much lossier than the other cavity mirrors. Replacing the flat LAYERTEC 143580 input coupler with the Y1-1025-0 will overcouple the cavity, broadening the linewidth and improve resolving the reflection dips and PDH error signal.

6 Reflection Dip and Error Signal with Revised Input Coupler

The flat input coupler was replaced with the Y1-1025-0 mirror to overcouple the cavity. Using the characterized transmittances, the cavity finesse was 9,250 and the linewidth was 42.5 kHz. This results in an analytical reflection dip of 42.0%, and an expected PDH error signal ampltidue of 451 mV, using a modulation index of 175 mrad.

The cavity was realigned, and a cavity was quickly formed with higher order mode flashing. Cavity alignment improved to the point where there was strong TEM_{00} flashing on the transmission camera, with a faint background of Laguerre-Gaussian modes. The TEM_{00} would intermittently switch to a higher order mode, but predominantly resided in the TEM_{00} mode.

6.1 Overcoupled Cavity Measurements

I modulated the pump with the EOM at 36.07 MHz with a modulation index of 175 mrad. Using the DC readout of the reflection PD for the reflection dips, and the RF PD port

for the PDH error signal, I recorded the reflection dip and PDH error signal as the pump frequency passively passed through resonance due to the laser's frequency noise and acoustic noise. Fig. 10 shows the measured reflection dip of 12.1% and PDH error signal with 20 mV amplitude. The measured reflection dip was lower than the analytical expectation of 42.0%, which could be due to mode mismatch. The measured PDH error signal is also lower than the analytical expectation of 451 mV; however, it is vastly larger than the previously recorded 100 μV. This larger error signal had a high-SNR of 45 dB and is more susceptible to locking the pump to the cavity.

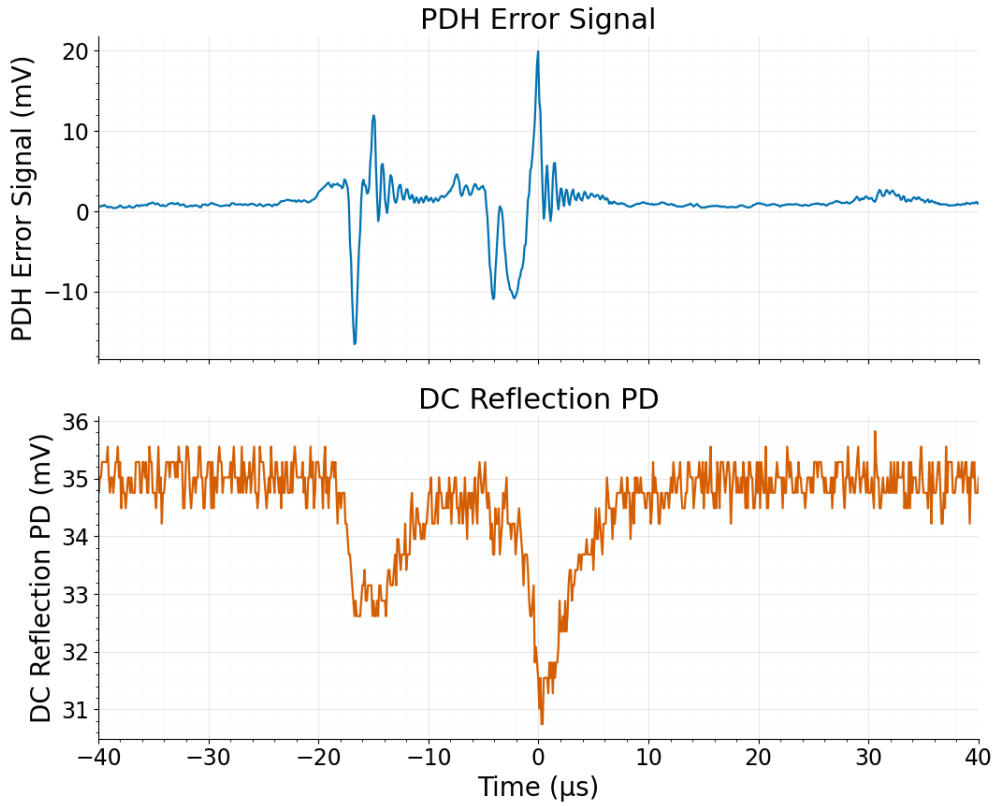


Figure 10: Measured reflection dip of 12.1% and PDH error signal with 20 mV amplitude.

While attempting to lock the pump to the cavity through modulating the laser diode, modulating the current seemed to have no effect on the error signal nor the laser current monitor display. This is suggestive that the diode laser's current driver is preventing external current modulation. Furthermore, a high-bandwidth current driver would suppress the laser's higher frequency noise and reduce the required loop bandwidth to lock the cavity, improving stability when using a FPGA controller with time delays on the order of a μs.

7 Conclusion

In this report, I have troubleshoted a cavity that will be used for cavity-enhanced SFG for 2 µm detection. Through troubleshooting the cavity, I have characterized the pump beam, optimized mode matching solutions for lens-displacement robustness, and characterized the

cavity mirrors' transmitances. This project highlights the importance of characterizing subsystems in an experimental setup due to their interdependencies. By measuring the cavity mirror transmittances, I reconciled the discrepancies between the expected and measured PDH error signal. Now, with the lossier input coupler, the measured reflection dip of 12.1% is much closer to the 42.0% expectation, and the PDH error signal is susceptible to locking. With this high SNR PDH error signal, a higher bandwidth diode laser current driver can lock the pump to the cavity. Then, the PPLN crystal can be inserted into the cavity along with a lossier input coupler to account for the PPLN pump absorption, and cavity-enhanced SFG can be observed.

References

[1] R. X. Adhikari, K. Arai, A. F. Brooks, C. Wipf, O. Aguiar, P. Altin, *et al.*, "A cryogenic silicon interferometer for gravitational-wave detection," *Classical and Quantum Gravity*, vol. 37, p. 165003, Jul. 2020.

[2] C. E. Vollmer, C. Baune, A. Samblowski, T. Eberle, V. Händchen, J. Fiurášek, and R. Schnabel, "Quantum Up-Conversion of Squeezed Vacuum States from 1550 to 532 nm," *Physical Review Letters*, vol. 112, p. 073602, Feb. 2014.

[3] R. Abbott, "EOM Driver," Tech. Rep. LIGO-D1200794-v3, LIGO Laboratory, California Institute of Technology and Massachusetts Institute of Technology, 2012. LIGO Document Control Center.

[4] E. D. Black, "An introduction to Pound–Drever–Hall laser frequency stabilization," *American Journal of Physics*, vol. 69, pp. 79–87, Jan. 2001.